Palaeogeography, Palaeoclimatology, Palaeoecology 600 (2022) 111082

Contents lists available at ScienceDirect

Palaeogeography, Palaeoclimatology, Palaeoecology

journal homepage: www.elsevier.com/locate/palaeo

OSL dating of coastal sand dunes in southeastern China provides new insights into the relationship between aeolian activity and eustatic sea-level fluctuations

Tongyan Lü [a,b], Jimin Sun [c,d,*], James K. Feathers [e], Dongxia Sun [a,b], Chenxu Cui [f], Xiaoli Shen [g]

[a] Key Laboratory of Neotectonic Movement and Geohazard, Ministry of Natural Resources, Beijing 100081, China
[b] Institute of Geomechanics, Chinese Academy of Geological Sciences, Beijing 100081, China
[c] Institute of Geology and Geophysics, Chinese Academy of Science, Beijing 100029, China
[d] University of Chinese Academy of Sciences, Beijing 100049, China
[e] Luminescence Dating Laboratory, University of Washington, Box 353412, Seattle, WA 98195-3412, USA
[f] China University of Geoscience, Beijing 100083, China
[g] College of Earth Science and Engineering, Shandong University of Science and Technology, Qingdao 266590, China

ARTICLE INFO

Editor: Paul Hesse

Keywords:
Coastal dunes
OSL dating
Climate change
Sea level
SE China

ABSTRACT

The southeastern coastal region of China has coastal sand dunes, which are usually called paleo-sand dunes or "Old Red Sandstone". The ages and geological implications of these coastal dunes have been studied for tens of years but are still controversial. In this paper, we used optically stimulated luminescence (OSL) dating to establish the chronology of the paleo-aeolian reddish sand dunes from two representative sites in the coastal region of SE China. Our results indicate that the sand dunes were mainly accumulated in three periods, including 9–6 ka (broadly corresponding to marine isotope stage (MIS) 1), 50–26 ka (MIS 3), and 110–74 ka (MIS 5). Based on the comparison between the regional aeolian dune records and the global sea-level fluctuations, we concluded that the reddish sand dunes were associated with the aeolian processes during interglacials and interstadials when sea-level were relatively higher compared with glacial maxima. We proposed a conceptual model to interpret the formation of the coastal sand dunes. We suggest that coastal dunes that formed during the glacial maxima could not be preserved in highstands above the present sea-level due to the lower altitude of sand dunes and the erosion by water waves during the subsequent marine transgression. Therefore, only aeolian sand dunes accumulated in higher altitudes during sea-level rise were preserved as in the coastal region of SE China.

1. Introduction

Coastal aeolian sand dunes are sensitive to climate change, serving as ideal geological archives for coastal evolution and paleo-environmental changes (Carter, 1991; Rust and Illenberger, 1996; Hansom, 2001; Woodroffe, 2002; Nel et al., 2014; Hamylton, 2017). Reddish coastal sand dunes usually occur in tropical and/or subtropical regions. The reddish color of sands is due to the iron oxide mineral coating on the surface of grains during intense chemical weathering in which iron is released from primary minerals to form free iron oxides mainly including goethite (FeOOH) and hematite (Fe_2O_3) (Walker, 1979; Gardner and Pye, 1981; Wopfner and Twidale, 1988; Pye and Tsoar, 2009; Roskin et al., 2012). The factors of rubification, including source factors, environmental conditions, and burial time, have been discussed by many authors (e.g., Walker, 1979; Besler, 2008; Tsoar et al., 2008, 2009; Roskin et al., 2012). The deposition of reddish coastal sand dunes is associated with sea-level fluctuations and thus can reflect coastal evolution and paleoclimate (e.g., Singhvi et al., 1986; Murray-Wallace, 2002; Bateman et al., 2004, 2011; Zhang et al., 2008; Quang-Minh et al., 2010; Tamura et al., 2011; Hu et al., 2012; Jayangondaperumal et al., 2012; Alappat et al., 2013; Jin et al., 2017, 2018).

Paleo-aeolian sand dunes can be found in the modern shoreline in SE China (Zhang et al., 1985; Wu and Wang, 2001; Zhang et al., 2008; Hu et al., 2012; Yu et al., 2014; Jin et al., 2017, 2018). Since the 1950s, many aspects of these sand dunes have been studied including sedimentology (Wu and Wang, 2001; Li et al., 2011; Yu et al., 2014; Lai et al., 2017), chronology (Wu, 1996; Zhang et al., 2008; Hu et al., 2012; Yu et al., 2014; Jin et al., 2017, 2018), and paleoclimate (Wang et al.,

* Corresponding author at: Institute of Geology and Geophysics, Chinese Academy of Science, Beijing 100029, China.
E-mail address: jmsun@mail.iggcas.ac.cn (J. Sun).

https://doi.org/10.1016/j.palaeo.2022.111082
Received 14 January 2022; Received in revised form 22 May 2022; Accepted 23 May 2022
Available online 27 May 2022

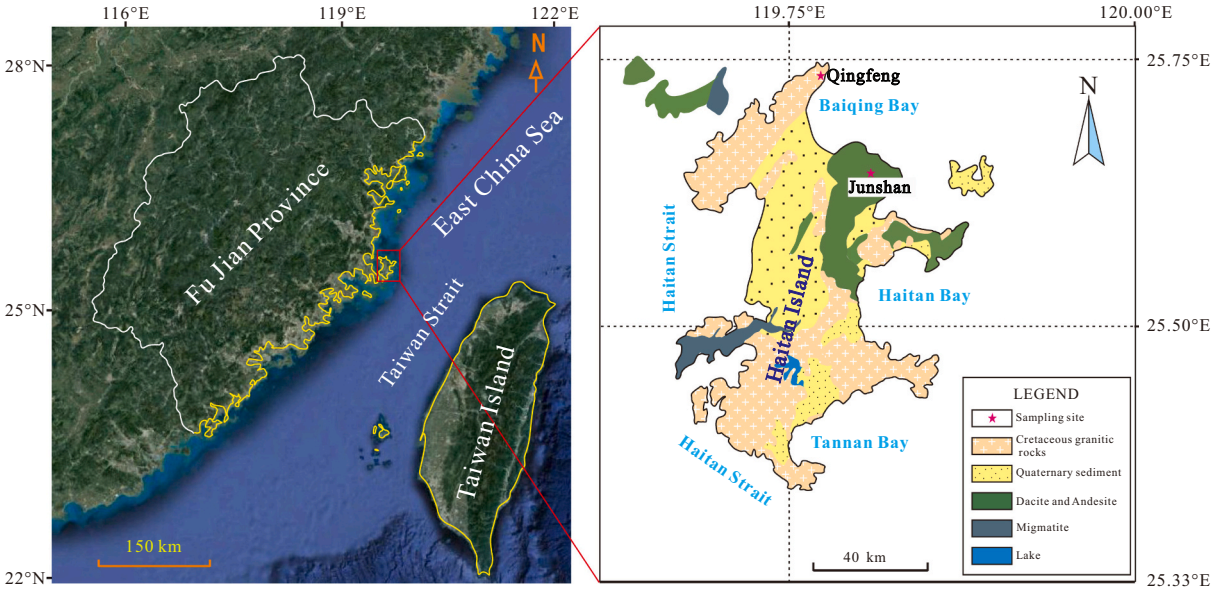

Fig. 1. Map shows the Haitan Island and the locations (red stars) of the Qingfeng and Junshan sections. (For interpretation of the references to color in this figure legend, the reader is referred to the web version of this article.)

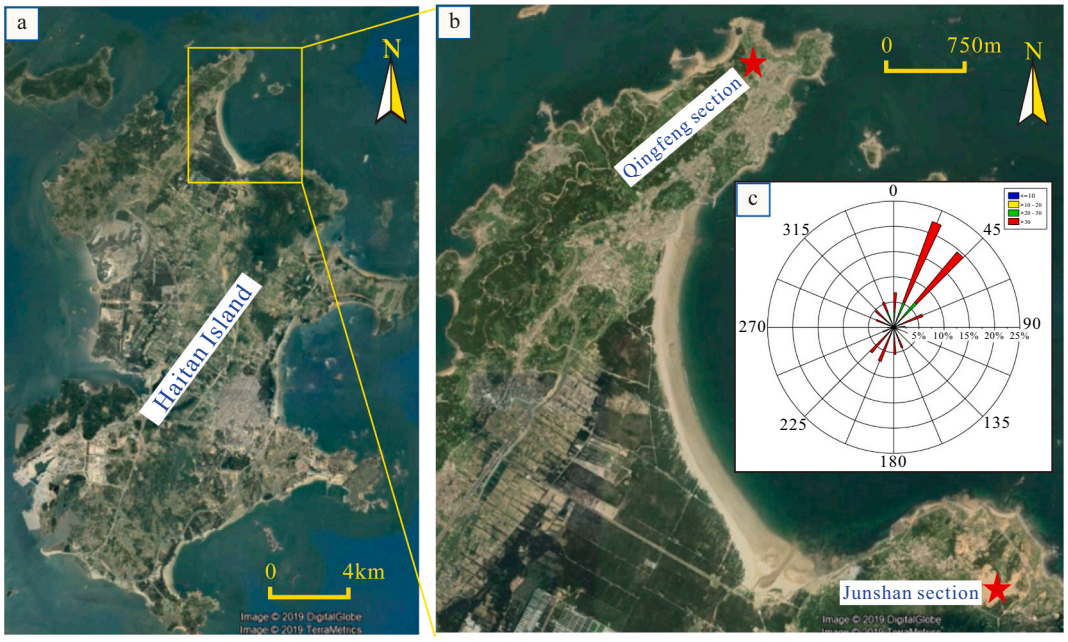

Fig. 2. (a) Goole Earth maps showing the locations of the Qingfeng and Junshan sections; and (b) The prevailing wind directions (the rose diagram) of the Haitan Island since 1950 (data from the National Meteorological Information Centre of China, http://data.cma.cn). (For interpretation of the references to color in this figure legend, the reader is referred to the web version of this article.)

2013; Shen et al., 2016). Although most previous researchers suggest that these reddish sediments are aeolian in origin, there are still many debates on their ages as well as the relationship with sea-level fluctuations. Based on climatostratigraphy (Yao et al., 1985; Zeng et al., 1999), radiocarbon dating (Wu, 1996; Zeng et al., 1999), and thermoluminescence (TL) dating (Zeng et al., 1999; Tan and Wu, 2001), the age of reddish sand dunes was reported to be 49–25 ka. However, there are shortcomings in these earlier dating. For example, the climatostratigraphy usually has low precision and with large uncertainties, the radiocarbon dating can only date the sediments younger than 50 ka, and the TL technique is now replaced by OSL dating. Although OSL dating has been used for these sand dunes (e.g., Jin et al., 2017, 2018; Zhang et al., 2008), there are uncertainties in some ages. Jin et al. (2017, 2018) dated the ages of the "old reddish sandstone" by using the single-aliquot regenerative-dose (SAR) protocol, which yielded an age range from 110 to 20 ka. However, details of the saturation of the OSL signal in the Qingfeng section were not shown, especially for some samples with D_e values of lager than 200 Gy (Jin et al., 2017). Zhang et al. (2008) reported OSL dating results of sand dunes on two terraces with ages of ~74 ka and ~ 3.5 ka, respectively. Unfortunately, the sand dunes on the highest terrace was not dated accurately due to an unreliable dose rate and thus was only inferred to be older than ~77 ka.

During the last two decades, the OSL dating of quartz and infrared stimulated luminescence (IRSL) of feldspar have been greatly improved

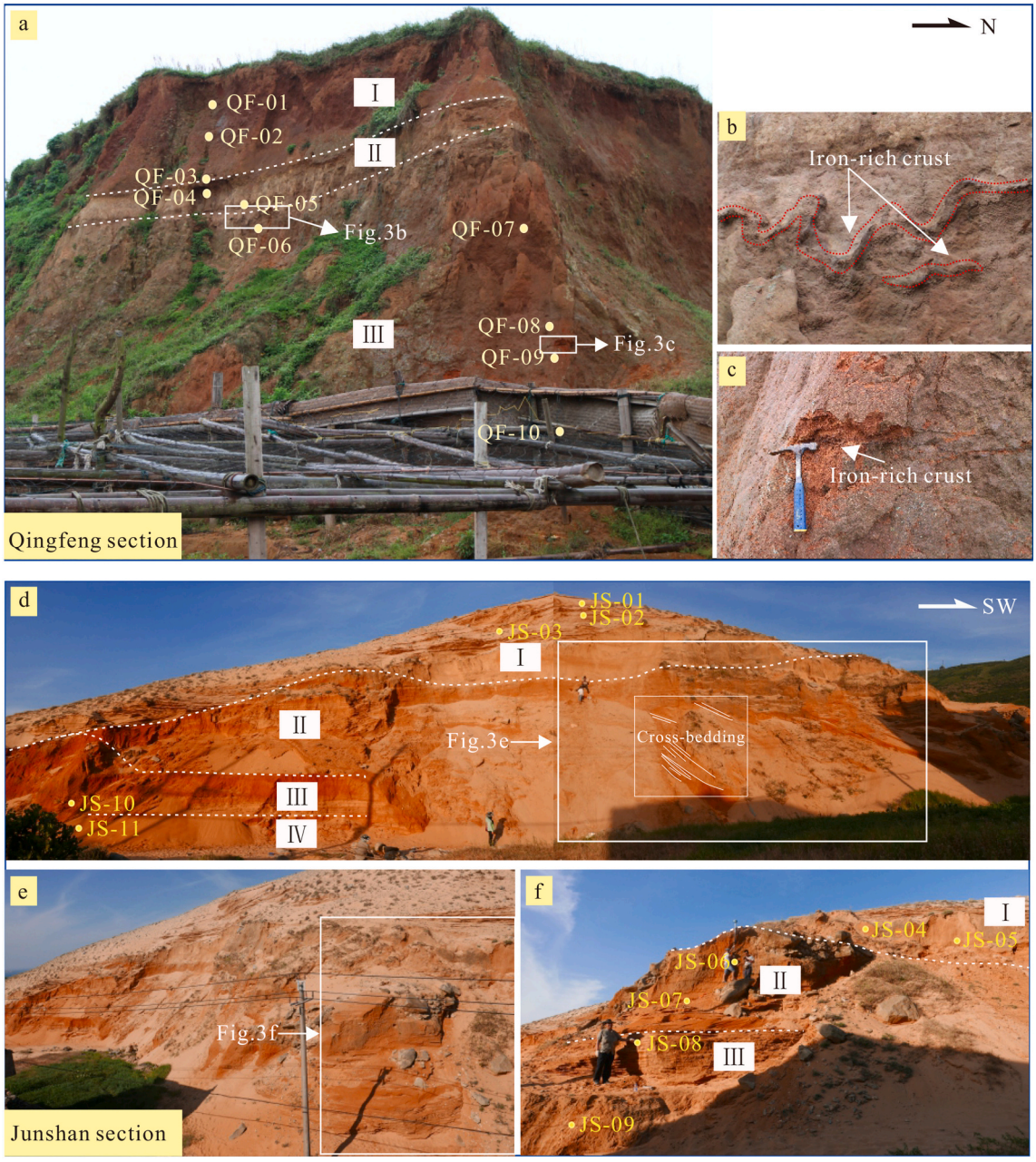

Fig. 3. Photographs show the outcrops and sampling positions of the Qingfeng (a-c) and Junshan sections (d-f). Iron-rich crusts are shown in Fig. 3b and c.

(e.g., Aitken, 1998; Murray and Wintle, 2000; Murray and Olley, 2002; Lai, 2006; Wintle and Murray, 2006; Li and Li, 2011, 2012; Kars et al., 2014; Li et al., 2014; Fu et al., 2020). The development of the SAR protocol (Murray and Wintle, 2000) has allowed accurate estimation of the equivalent dose (D_e) of quartz and thus has been widely applied in OSL dating. For older deposits, potassium-feldspar (K-feldspar) is a better mineral than quartz because it has a higher luminescence saturation dose. To overcome the anomalous fading of the IRSL signal of feldspar, the post-IR IRSL (Buylaert et al., 2009; Kang et al., 2010; Thiel et al., 2011; Roberts, 2012; Kars et al., 2014; Wang et al., 2014; Madsen and Liu, 2018) and Multi-Elevated-Temperature post-IR IRSL (MET-pIRIR) dating methods (Li and Li, 2011, 2012; Li et al., 2013) have been developed to isolate a non-fading IRSL signal. Using these new techniques, quartz and K-feldspar dating can provide accurate results and a longer chronology for a wide range of depositional environments.

In this study, both the SAR (quartz) and MET-pIRIR (K-feldspar) dating techniques were used in order to date ages of the coastal dunes in SE China. The aims of this paper are: (1) to provide a luminescence chronology of coastal dunes from two sections; (2) to understand the relationship between the accumulations of reddish aeolian dunes and the eustatic sea-level fluctuations; (3) to discuss the aeolian processes of episodic dune buildings in the coastal area.

2. Geological setting, materials, and methods

2.1. Geological setting

The study area is located in the Haitan Island in the Fujian Province of SE China, which is separated from Taiwan by the Taiwan Strait (Fig. 1).

The Haitan Island has a subtropical climate, which is controlled by the East Asian monsoon characterized by hot/humid summer and mild/dry winter. The mean annual precipitation (averaged from 1981 to 2010) is about 1300 mm (National Meteorological Information Centre,

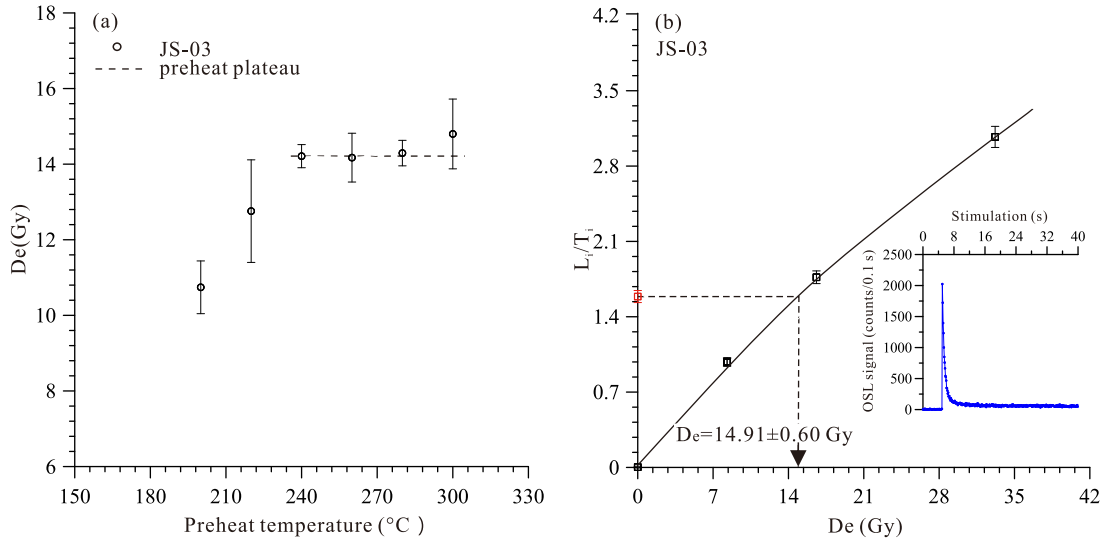

Fig. 4. (a) Equivalent dose as a function of preheat temperature; (b) Representative SAR growth curve for an aliquot of sample JS-03. The black squares and red square indicate representative and natural signals, respectively, which have been sensitivity-normalized. The equivalent dose is indicated by arrow. The inset figure shows a typical rapidly decaying signal occurring during optical stimulation (open blue circles). (For interpretation of the references to color in this figure legend, the reader is referred to the web version of this article.)

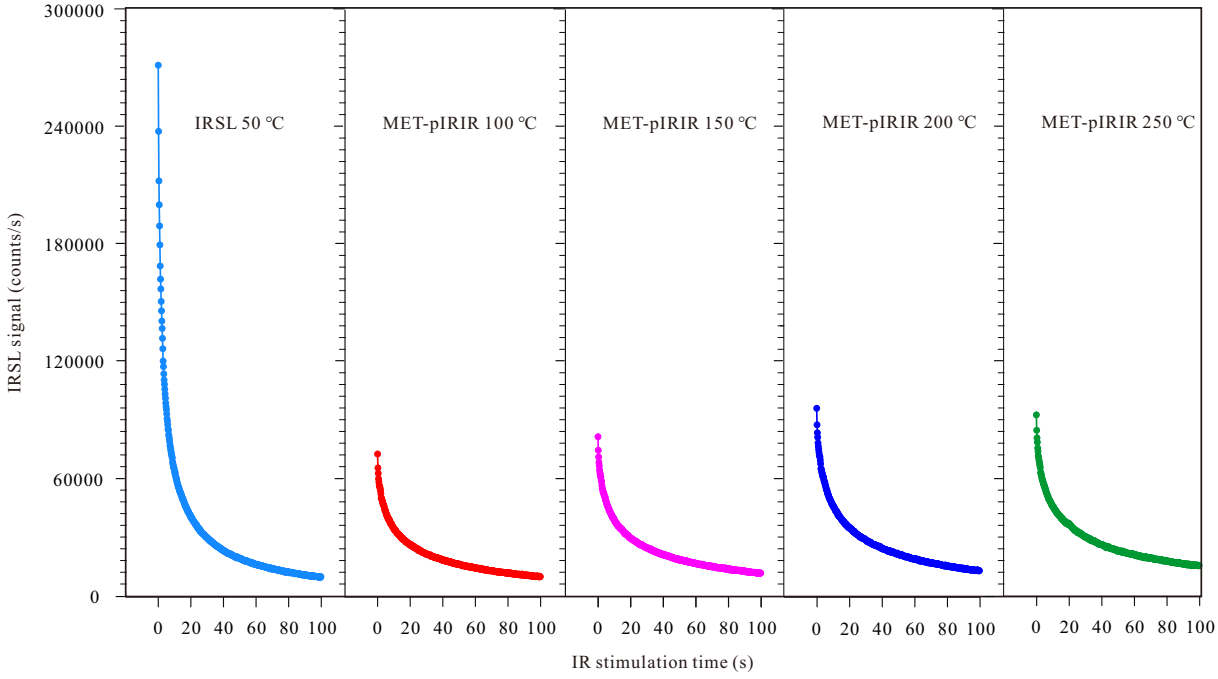

Fig. 5. Typical IRSL and MET-pIRIR decay curves of sample QF-10 measured at different stimulation temperatures.

http://data.cma.cn). The specific geographic location of this island (facing to the Taiwan Strait) results in frequent strong winds, with an average wind speed of 17.3 km/h (National Meteorological Information Centre, http://data.cma.cn). The local maximum instantaneous wind speed can be up to 30 m/s and the main directions are NNE and NE (data from the National Meteorological Information Centre, http://data.cma.cn) (Fig. 2).

On Haitan Island, paleo-aeolian sand dunes occur either as isolated outcrops or as overlapped dune ridges parallel to the coast. These dunes can be up to 10 km long with elevations of 7 to 90 m above sea level. The Qingfeng (25°39.76′ N, 119°46.77′ E) and Junshan (25°36.72′ N, 119°48.34′ E) sections are located in the northeastern corner of the Haitan Island (Fig. 2a), facing to the Taiwan Strait in the east. The Qingfeng section is a relict paleo-sand dune accumulated on the top of granites in the northeastern corner of the island; and the Junshan section is on the windward slope of coastal hills (Fig. 2b).

2.2. Materials

The Qingfeng section has a basal elevation of 21 m above sea level, and it has a thickness of 12 m (Fig. 3a). Three beds (I to III) were identified based on the color, size and sedimentary textures. The top unit of this section (Unit I) is a reddish-brown sand bed (from top to a depth of 3.3 m) which has a massive structure. Underlying this bed, there is a 2.3 m-thick light-yellow fine-grained pedogenic layer (Unit II), which is characterized by the existence of irregular dark-brown iron-rich

Table 1
Sample depths, dose rates and optical dating results[a,b]

Serial No.	Sample	Depth (m)	U (ppm)	Th (ppm)	K (%)	Water (%)	U/Th ratio	D_e (Gy)	Number	Cosmic ray (Gy/ka)	Dose rate (Gy/ka)	Central age (ka)
1	QF-01	1.0	1.76	9.31	1.43	10	0.19	34.7 ± 1.4	22	0.18 ± 0.04	2.47 ± 0.15	14.1 ± 1.0
2	QF-02	1.5	1.85	8.92	1.55	5	0.21	71.8 ± 2.4	23	0.17 ± 0.03	2.69 ± 0.17	26.7 ± 1.9
3	QF-03	3.3	0.98	5.22	1.41	4	0.19	100.3 ± 3.5	25	0.14 ± 0.03	2.10 ± 0.15	47.8 ± 3.7
4	QF-04	3.6	2.41	12.20	1.98	11	0.20	130.7 ± 5.2	21	0.12 ± 0.03	3.18 ± 0.20	41.1 ± 3.0
5	QF-05	4.5	1.66	8.91	1.71	10	0.19	130.9 ± 8.4	26	0.11 ± 0.02	2.60 ± 0.17	50.4 ± 4.6
6	QF-06	5.1	1.62	8.14	1.53	11	0.20	116.9 ± 5.7	16	0.11 ± 0.02	2.36 ± 0.15	49.6 ± 4.0
7	QF-07 (Quartz)	6.0	1.49	7.55	1.44	7	0.20	173.2 ± 5.3	19	0.10 ± 0.02	2.29 ± 0.15	75.4 ± 5.4
8	QF-07 (K-feldspar)	6.0	1.49	7.55	1.44	7	0.20	309.1 ± 15.3	13	0.10 ± 0.02	2.86 ± 0.23	108.1 ± 10.4
9	QF-08	8.3	1.51	8.31	1.41	9	0.18	164.2 ± 7.7	14	0.08 ± 0.02	2.26 ± 0.14	72.7 ± 5.7
10	QF-09	9.5	1.59	8.07	1.47	13	0.20	165.0 ± 6.9	20	0.08 ± 0.02	2.21 ± 0.14	74.4 ± 5.7
11	QF-10 (Quartz)	11.9	1.41	5.68	1.65	5	0.25	209.7 ± 10.1	18	0.07 ± 0.01	2.36 ± 0.17	88.5 ± 7.5
12	QF-10 (K-feldspar)	11.9	1.41	5.68	1.65	5	0.25	515.7 ± 27.2	9	0.07 ± 0.01	2.93 ± 0.24	175.9 ± 16.9
13	JS-01	0.2	0.66	3.21	1.20	6	0.21	12.3 ± 0.5	19	0.22 ± 0.05	1.72 ± 0.13	7.2 ± 0.6
14	JS-02	0.5	0.49	2.40	1.17	5	0.20	10.5 ± 0.5	16	0.20 ± 0.04	1.60 ± 0.12	6.6 ± 0.6
15	JS-03	7.5	0.56	3.32	1.36	3	0.17	13.7 ± 0.4	22	0.09 ± 0.02	1.81 ± 0.14	7.6 ± 0.6
16	JS-04	8.0	0.48	2.24	1.15	7	0.21	11.2 ± 0.2	24	0.09 ± 0.02	1.43 ± 0.11	7.8 ± 0.7
17	JS-05	12.0	0.61	3.47	1.40	9	0.18	14.4 ± 0.5	18	0.06 ± 0.01	1.71 ± 0.13	8.4 ± 0.7
18	JS-06	14.0	0.90	4.58	1.99	11	0.20	95.8 ± 3.5	24	0.05 ± 0.01	2.34 ± 0.17	41.0 ± 3.4
18	JS-07	15.0	0.65	3.28	2.11	6	0.20	117.8 ± 9.4	17	0.05 ± 0.01	2.44 ± 0.19	48.3 ± 5.4
19	JS-08	16.0	0.55	3.22	1.32	8	0.17	126.7 ± 5.0	20	0.05 ± 0.01	1.62 ± 0.07	78.4 ± 4.6
20	JS-09	20.7	1.31	6.87	1.64	14	0.19	147.0 ± 2.8	18	0.03 ± 0.01	2.16 ± 0.09	68.0 ± 3.7
21	JS-10	19.0	1.20	6.24	1.33	5	0.19	170.3 ± 6.9	20	0.04 ± 0.01	2.02 ± 0.14	84.2 ± 6.7
22	JS-11	23.0	0.74	3.65	1.50	5	0.20	193.8 ± 7.2	18	0.03 ± 0.01	1.91 ± 0.15	101.2 ± 8.6

[a] Equivalent dose determined by the single aliquot regenerative dose method under blue light excitation (470 nm) (Murray and Wintle, 2003) on the 90–125 μm quartz fraction. Central age model of Galbraith et al. (1999) was used.
[b] The analytical errors are within ±10‰ for the U, Th, and K contents and ± 5‰ for water content.

(ferritic) crust (hematite and/or goethite) at its base (Fig. 3b). The iron crust was due to the prolonged chemical weathering and the oxidation of Fe^{2+} (iron) to Fe^{3+}. The lowest part of the section (Unit III) is a dark reddish sand bed with iron crust at a depth of 9 m (Fig. 3c). The positions of the OSL samples are shown in Fig. 3a.

The Junshan section is located on the windward slope of the local Junshan Hill, which is 600 m west of the present coastline (Fig. 2b). It is a mega paleo-sand ridge with a height of 93 m (Fig. 3d). Four units (I to IV) can be subdivided according to sedimentary features. The uppermost unit is characterized by yellowish loosely accumulated sands, being different from the other underlying reddish sands. Five samples (JS-01, JS-02, JS-03, JS-04, and JS-05) were collected from different layers of this unit (Figs. 3d, f). The second unit (II) is a relict reddish-brown sand bed which has cross-bedding structure with an angle of repose of 33° (Fig. 3d). Two samples (JS-06 and JS-07) were collected from this unit (Fig. 3f). The third unit (III) is a more reddish sand bed. Three samples were collected from this unit (JS-08, JS09 and JS-10) (Figs. 3d, f). The lowest part of the section (unit IV) is characterized by the most reddish (brick-red) color, and the OSL sample of JS-11 was collected from this unit (Fig. 3d).

3. Methods

Samples were collected by using stainless steel tubes (5 cm in diameter and 25 cm long) to avoid exposure to sunlight. A 3 cm layer was removed in each outcrop to avoid any exposure to sunlight, and then the tube was hammered into the outcrop. When the tube was taken out, its two ends were covered by black-plastic bags. They were opened in the laboratory under subdued red light, and the samples in both ends of each tube were used for the measurements of water content and concentrations of U, Th, and K. The innermost portion was treated with 10% hydrochloric acid (HCl) to dissolve carbonates and iron oxides, and 10% hydrogen peroxide (H_2O_2) was used to remove organic matter. Then the 90–125 μm fraction was obtained by dry sieving. K-feldspar grains were separated using the heavy liquid of sodium polytungstate with a density of 2.58 g/cm^3. Subsequently, they were immersed in 10% hydrofluoric acid (HF) for 10 min to clean grains and also to remove the layer at the grain surface irradiated by external alpha particles (Li and Li, 2012). The quartz-rich fraction was separated by using heavy liquids with different densities (2.62 and 2.75 g/cm^3) and subsequently etched using 40% HF for about 40 min to remove feldspar contamination and the outer part of grains which is affected by alpha radiation (Mejdahl and Christiansen, 1994). Both K-feldspar and quartz grains were cleaned by using 10% HCl and high-purity water to remove any residual fluorides after etching before final drying. The purity of quartz was checked by examining the absence of the feldspar contamination using IRSL (Duller, 2003) and the 110 °C peak (Li et al., 2002). Separated K-feldspar and quartz grains were mounted on the center of each aluminum disc (9.8-mm-diameter) with silicon oil.

The pretreatment and OSL measurements were carried out in the Luminescence Dating Laboratory, at the Institute of Geology and Geophysics, Chinese Academy of Science by using an automated Risϕ

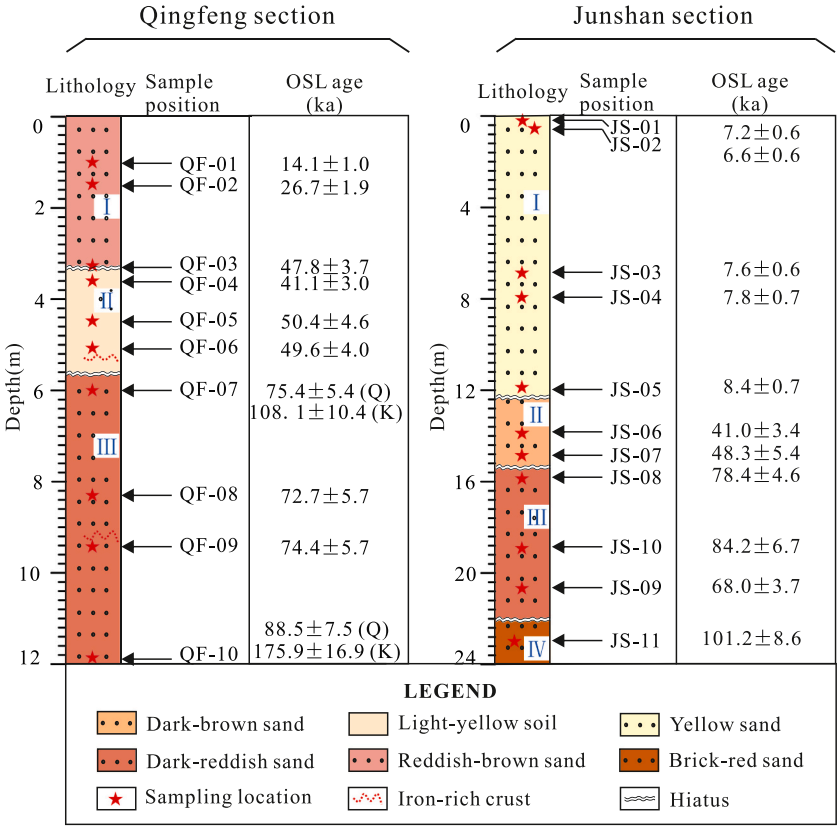

Fig. 6. Profiles of the Qingfeng and Junshan sections, the sampling positions and the OSL ages are also shown.

TL/OSL DA 15 reader with a $^{90}Sr/^{90}Y$ beta source. The IR laser diode (λ = 830 ± 10 nm) and the blue light emitting diodes (LED) (λ = 470 ± 30 nm) deliver up to 400 W/cm^2 and 50 W/cm^2 respectively, but only 90% of their full powers were used for stimulation. For SAR measurement, the emission was collected through a Hoya U-340 (λ = 7.5 mm) filter. SAR emission was integrated over the first 0.5 s of stimulation out of 40 s of measurement and the background was based on emissions for the last 2 s interval. For all the IRSL measurement, filters of Schott BG-39 and Corning 7–59 were placed in front of the photomultiplier tube to restrict transmission from UV to blue (320–480 nm). The first 1.4 s integral of the initial decay curves minus background, estimated from the last 4 s integral of the 100 s stimulation was used for D_e calculation.

The quartz equivalent dose was acquired by using the SAR protocol of Murray and Wintle (2000). The pre-heating temperature experiment was performed to evaluate the effect of temperature on thermal transfer of the regenerative signal prior to the application of SAR dating protocol (Murray and Wintle, 2003). A preheat temperature of 240 °C for 10 s was determined for the regeneration and a cut-heat to 220 °C for the test dose OSL measurements (Fig. 4a). Moreover, a zero dose was used for monitoring recuperation effects. Additionally, a repeat dose, same as the first regeneration dose, was used for checking the reproducibility of sensitivity correction (i.e. recycling ratio). Aliquots with recuperation higher than 5% or recycling ratio beyond the range of 1.0 ± 0.1 were discarded for age calculations. Using one aliquot of JS-03 as an example, Fig. 4b shows the OSL signal growth and decay curves. The shape of the OSL decay curve indicates grains are dominated by the fast component (Li and Li, 2006; Steffen et al., 2009). A first-order exponential function was used to fit the growth curve and then to yield an estimate of D_e (Murray and Wintle, 2000).

We also applied MET-pIRIR protocol (Li and Li, 2011, 2012) to date the K-feldspar grains of the coastal dunes. In such protocol, the IRSL signals of K-feldspar were measured by progressively increasing the IR stimulation temperature from 50 to 300 °C in steps of 50 °C. These IRSL signals at different stimulation temperatures were termed as the MET-pIRIR signals (Li and Li, 2011, 2012). The MET-pIRIR protocol has been tested and applied to aeolian sediments in northern China (Li and Li, 2011, 2012; Fu et al., 2012; Fu and Li, 2013; Lü et al., 2018). In this study, we applied a MET-pIRIR protocol which was improved by Li and Li (2011, 2012). For samples of QF-07 and QF-10, thirteen and fifteen aliquots were measured respectively. A preheat at 320 °C for 60 s was used for both regenerative and test dose IRSL measurements. The IRSL signals from regenerative doses were measured and each measurement was obtained by increasing the stimulation temperature in steps of 50 °C. Typical decay curves of the MET-pIRIR signals of sample QF-10 are shown in Fig. 5. The initial intensity of IRSL at 50 °C is the strongest, and the others have lower values. Then a "hot" IR bleaching at 325 °C for 100 s followed the end of the IRSL measurements for each test dose in order to minimize the residual signal.

The environmental dose rate is an estimation of sediment exposure to ionizing radiation from uranium, thorium, potassium, and cosmic sources after deposition (Table 1). Uranium and thorium concentrations were measured by using Inductively Coupled Plasma Mass Spectrometry (ICP-MS) (Bailey et al., 2003), whereas the potassium content was analyzed using Atomic Absorption Spectrophotometry (AAS) method (Williams et al., 1962) at the Analytical Laboratory, Beijing Research Institute of Uranium Geology. The concentrations of uranium, thorium, and potassium were converted into beta and gamma dose rates (Guérin et al., 2011). The cosmic dose rate is calculated considering the sample's geographic location, altitude and depth (Prescott and Stephan, 1982; Prescott and Hutton, 1994). The internal dose rate of K-feldspar was calculated using a K concentration of 13 ± 1% and a Rb content of 400 ± 100 ppm (Huntley and Hancock, 2001; Zhao and Li, 2005; Li et al., 2008).

Moreover, in order to study the origin of dune sands, microstructures of quartz grains were examined by using a scanning electron microscopy microscope. Quartz grains extracted from two samples

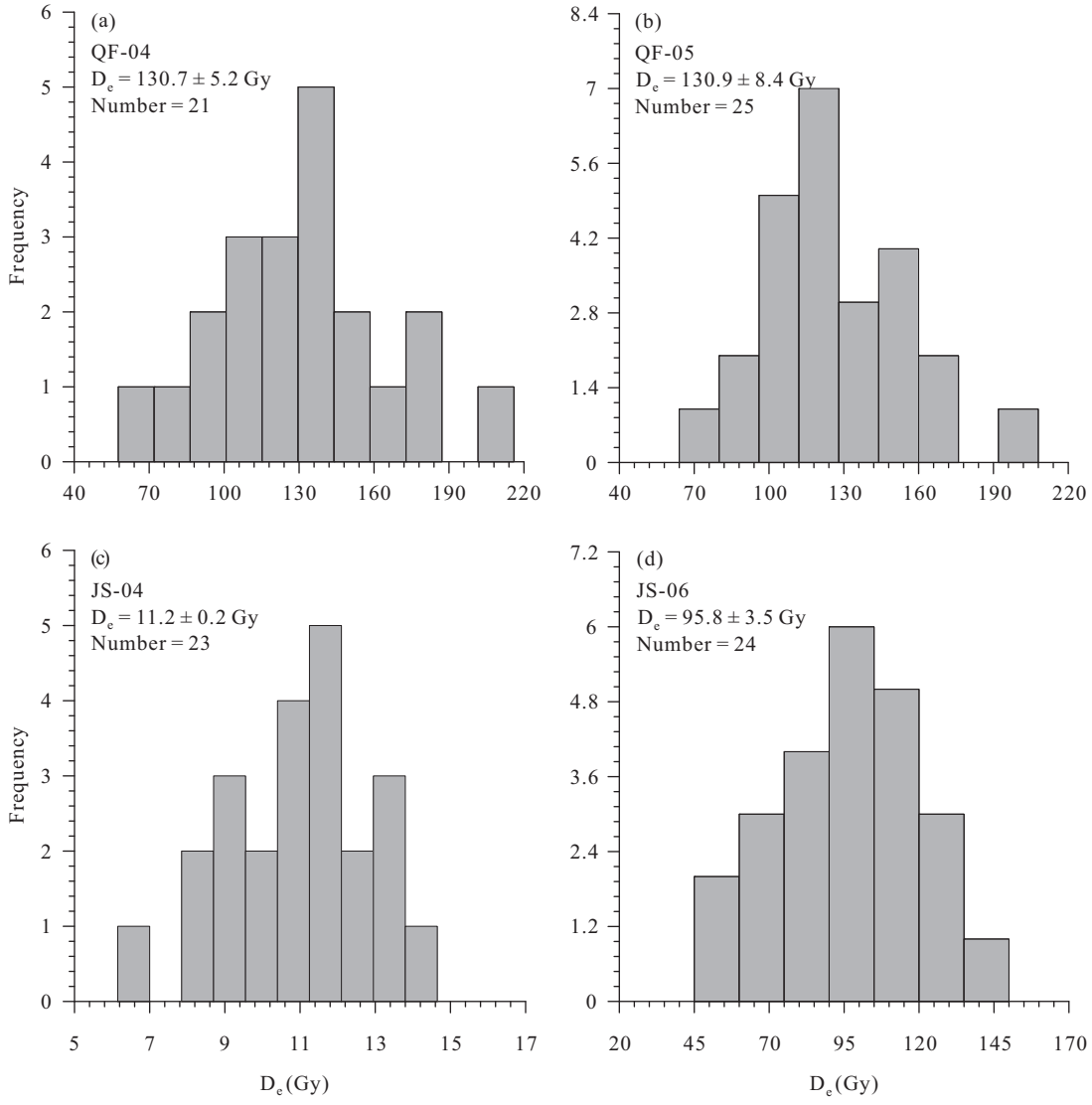

Fig. 7. The histograms of D_e distribution of samples QF-04 (a), QF-05 (b), JS-04 (c) and JS-06 (d).

(QF-06 and JS-08) were dispersed in alcohol, mounted on glass-topped stubs, gold-coated, and examined under an AM-Ray 1000B scanning electron microscopy equipped with energy dispersive X-rays.

4. Results

4.1. OSL chronologies of the Qingfeng and Junshan sections

The OSL ages of 22 samples are shown in Table 1 and Fig. 6. In order to check the reliability of OSL ages, histograms of the D_e distribution of four samples (QF-04, QF-05, JS-04, and JS-06) are shown in Fig. 7. All these examples have D_e values that show a normal distribution. The other samples have similar D_e distributions.

Ten samples from Qingfeng section were dated (Fig. 6). The ages of these samples can be divided into 4 groups. QF-01 and QF-02, obtained from the uppermost unit (I), have OSL ages of 14.1 ± 1.0 ka and 26.7 ± 1.9 ka, respectively. The age of the pedogenic layer (unit II) ranges from 50.4 ± 4.6 to 41.1 ± 3.0 ka (QF-03, QF-04, QF-05, QF-06). Three samples (QF-07, QF-08, QF-09) from the upper part of the third unit have similar OSL ages of approximate 75 ka (overlapping each other). At the bottom of this unit, the quartz OSL dating of sample QF-10 yielded an age of 88.5 ± 7.5 ka. However, the luminescence signals of quartz from 12 discs (67%) of QF-10 were saturated (Fig. 8a). Therefore, quartz was replaced by K-feldspar to date the age of QF-10 because the luminescence signals of K-feldspar saturate at a much higher level than quartz. K-feldspar De estimations at the six stimulation temperatures (e.g. 50, 100, 150, 200, 250, 300 °C) were yielded (Fig. 8b). They were converted to ages and plotted in Fig. 8b. In the MET-pIRIR age plot, the age values increase progressively from 50 to 200 °C, while constant and statistically indistinguishable age values were obtained for the MET-pIRIR signal from 200 to 300 °C. Therefore, the age of this sample is about 175.9 ± 16.9 ka at 200 °C. Moreover, QF-07 was also dated using MET-pIRIR protocol in order to check the accuracy of the K-feldspar age of QF-10, although the quartz luminescence signals of sample QF-07 were not saturated (Fig. 8c). We used the same procedure as the sample QF-10 and observed an age plateau between the stimulation temperatures of 200–250 °C (Fig. 8d), which yielded a K-feldspar age of 108.1 ± 10.4 ka. Obviously, this age is about 32.7 kyr older than the quartz OSL age. Multiple hypotheses have been proposed to account for the age overestimation of K-feldspar (Zhang and Li, 2020), such as signal inheritance (Colarossi et al., 2018; Liu et al., 2016), thermally transferred signal (Nian et al., 2012; Qin and Zhou, 2012), and dose dependent sensitivity change (Li and Li, 2013; Fu et al., 2015). Given these uncertainties, we suggest that the K-feldspar age of QF-10 may be used as a maximum age.

In the Junshan section, the OSL dating results of eleven samples are

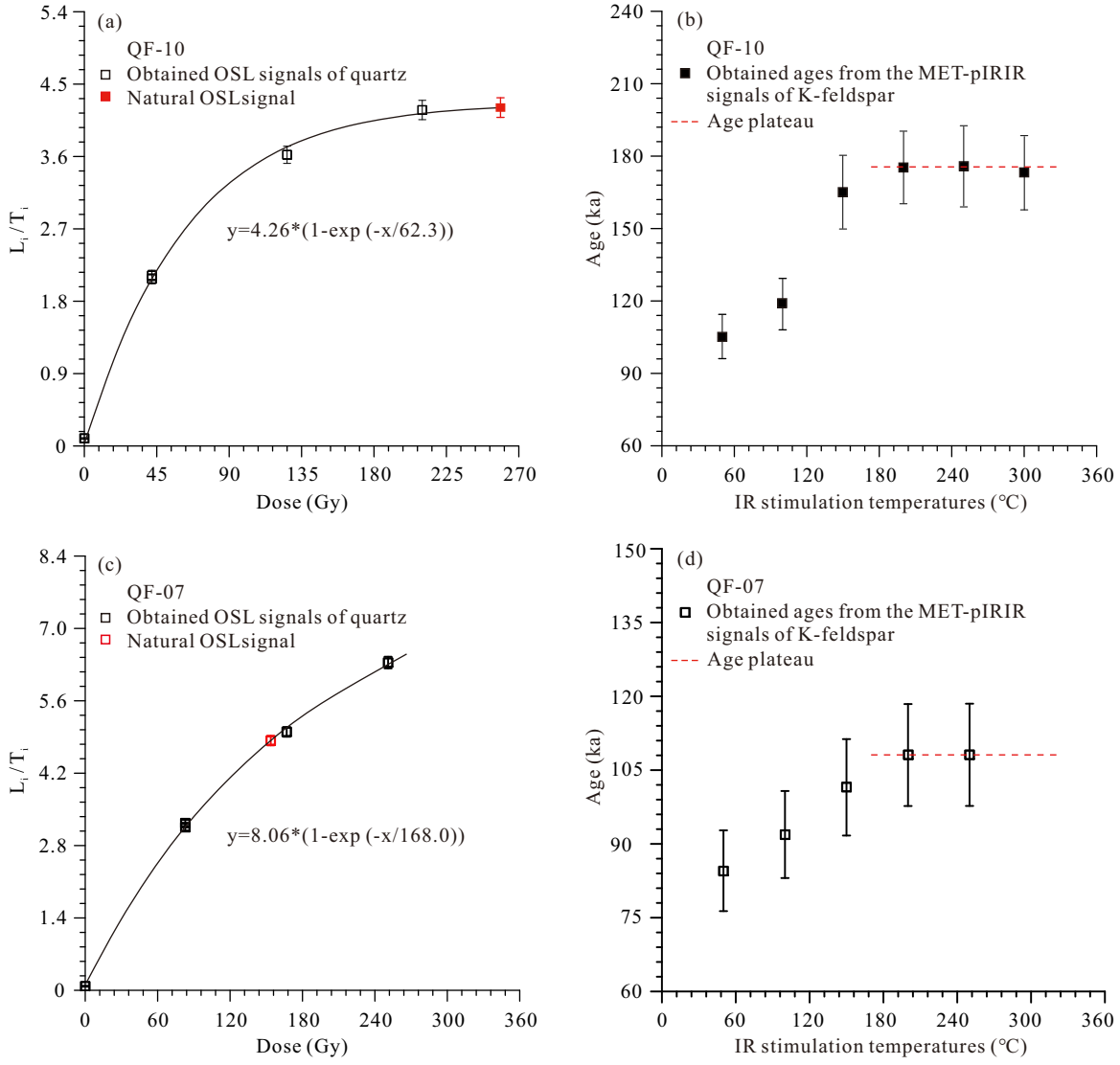

Fig. 8. (a) The characteristic dose saturation level of the dose response curve of quartz grains of sample QF-10, using the SAR protocol. The data points were fitting using a single saturating exponential function; (b) MET-pIRIR ages of sample QF-10 obtained using the MET-pIRIR protocol of K-feldspar. Ages tend to increase as the stimulation temperature increased from 50 to 200 °C, showing an age plateau from 200 to 300 °C; (c) The dose response curve of quartz grains of sample QF-07, using the SAR protocol; (d) MET-pIRIR ages of sample QF-07 of K-feldspar.

also shown in Fig. 6. All the five samples of Unit I (JS-01, JS-02, JS-03, JS-04, and JS-05) have similar ages of 8–6 ka (Fig. 6). Two samples (JS-06 and JS-07) of Unit II have OSL ages of 48–41 ka. Three samples of Unit III (JS-08, JS-09, and JS-10) have ages ranging from 84 to 68 ka. One sample of Unit IV (JS-11) has an age of 101.2 ± 8.6 ka.

4.2. Scanning electron microscopy analysis

Scanning electron micrographs of quartz grains from samples QF-06 (Figs. 9a, b) and JS-08 (Figs. 9c, d) are shown in Fig. 9. The particle sizes of quartz from these two sections range from 100 to 300 μm, but mostly having diameters of ca. 250 μm. Most of the quartz grains have sub-rounded shapes (Fig. 9a-d) and commonly have typical dish-shaped depressions (Fig. 9a to c). The above sedimentary features are characteristics of aeolian transportation (Mckee, 1979).

5. Discussions

5.1. The reliability of the dose rate

Chemical weathering is considered to be an important factor for dose rate measurement in luminescence dating (Olley et al., 1996; Jeong et al., 2007; Zhang et al., 2008, 2019; Jin et al., 2018, 2021). When the sediments experience strong chemical weathering, the mobile elements will be leached. The chemical weathering may cause secular disequilibrium in the uranium and thorium decay series after deposition. In most weathered sediments, thorium is regarded as a highly immobile element and the ^{232}Th decay chain is expected to be in secular equilibrium in most natural materials during weathering (Braun et al., 1993; Olley et al., 1996). Compared with thorium, uranium is relatively mobile (Mathieu et al., 1995; Olley et al., 1996; Dequincey et al., 2002; Chabaux et al., 2003). Usually, the U/Th ratio can be used to judge the equilibrium conditions in sediments. Stronger chemical weathering corresponds to a decreasing ratio of U/Th (Zhang et al., 2008, 2019; Jin et al., 2018, 2021). We calculated the U/Th ratios in the Qingfeng and Junshan sections (Table 1). Our results show that 95.5% of the U/Th

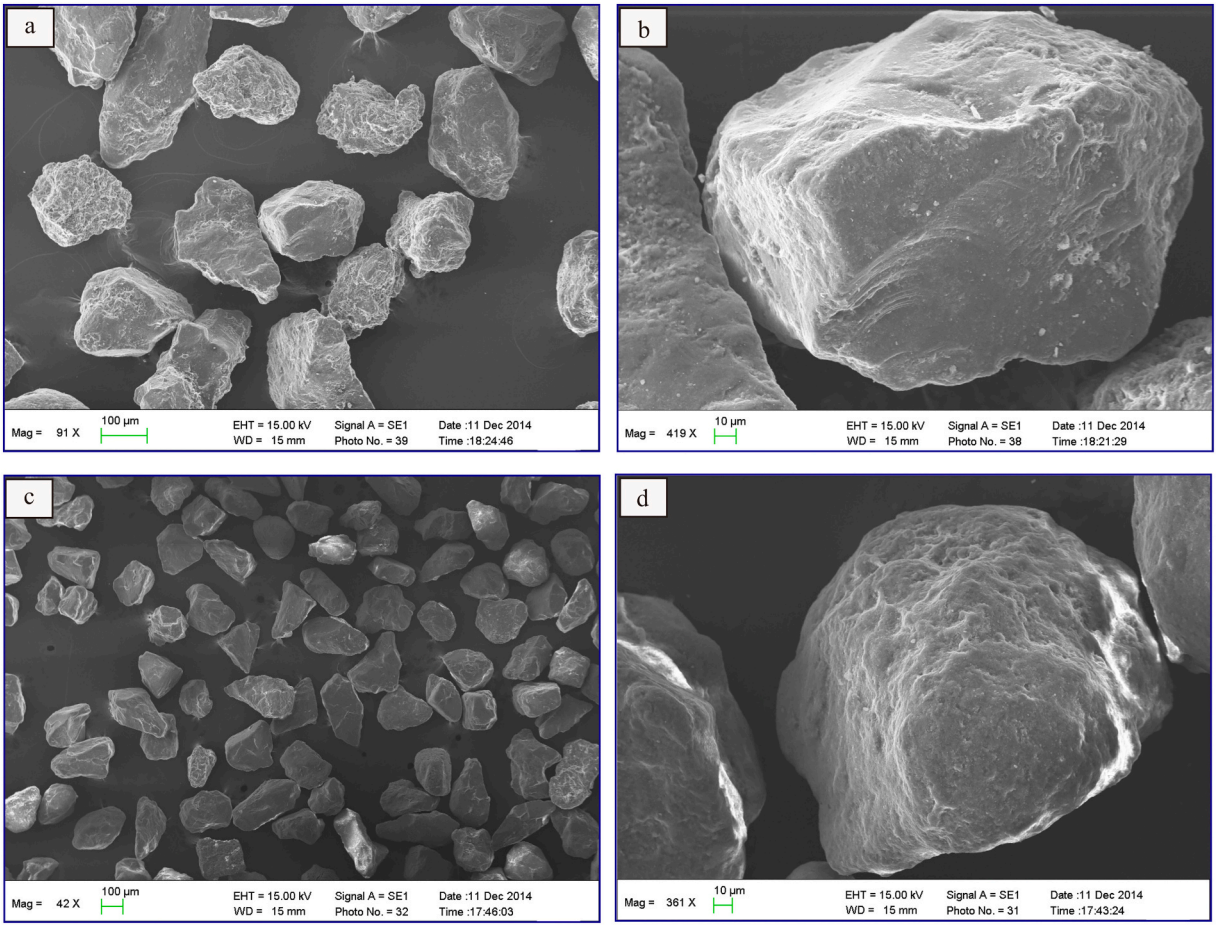

Fig. 9. Scanning electron micrographs of quartz grains of samples QF-06 (a, b) and JS-08 (c, d).

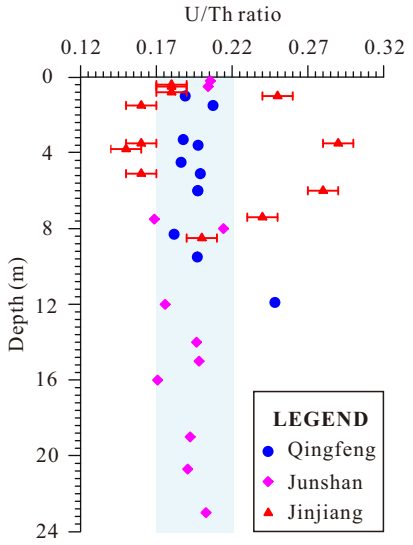

Fig. 10. U/Th ratios versus depth of samples from the Qingfeng, Junshan and Jinjiang sections. Data of the Jinjiang section is from Zhang et al., 2008.

ratios are in the range of 0.17 and 0.22. This narrow range of values is more homogenous compared to those of Zhang et al. (2008) (Fig. 10). Although the U and Th contents in the Qingfeng section are greater than the samples in the Junshan section, the U/Th ratios are very similar. We suggest that although the samples might have experienced some

Fig. 11. Photo shows the climbing sand dunes on the windward slope of the Junshan Hill.

chemical weathering, the nearly homogenous U/Th ratios imply that effect of the past chemical weathering on the dose rate was not significant.

5.2. *Aeolian origin of the paleo-sand dunes*

The origin of the reddish sand dunes of SE China has a long history of debate since the 1960s (e.g., Yao et al., 1985; Zhang et al., 1985; Wang et al., 1998; Zeng et al., 1999; Lai et al., 2017). One view is that these sands were transported by wave or tide and deposited in a proximal

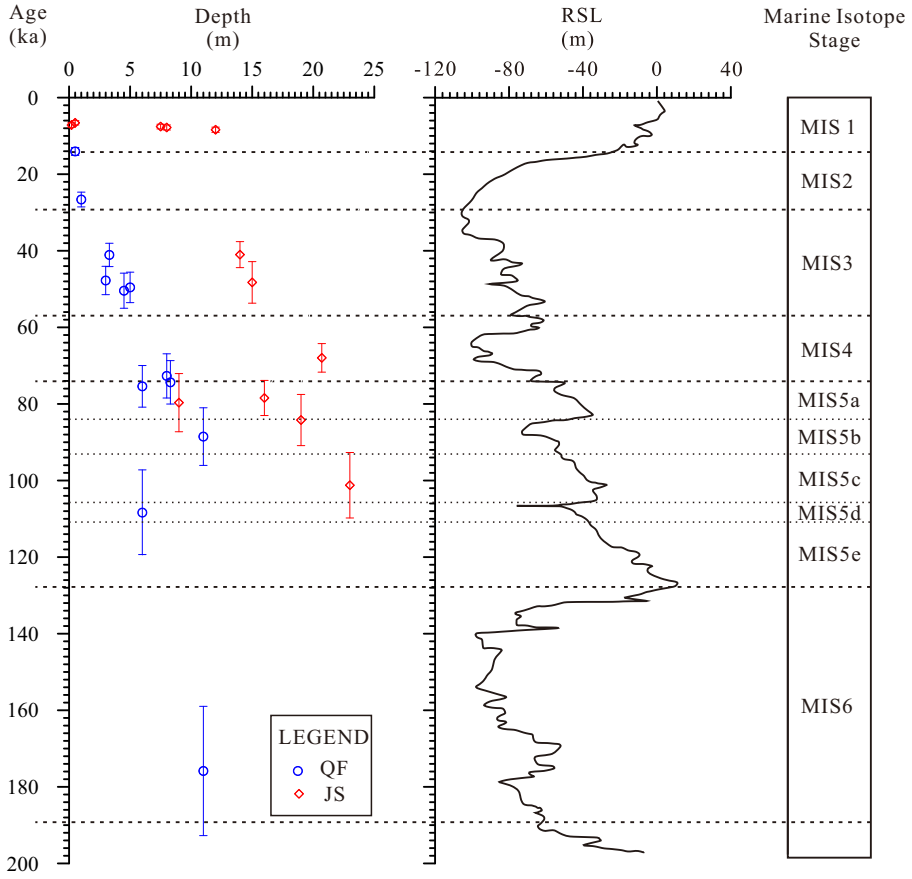

Fig. 12. Relationship between OSL ages, relative sea level and marine isotope stages. Plots of OSL ages versus depth of Qingfeng and Junshan sections are shown in the left. Data of the relative sea level curve are from Grant et al. (2012, 2014).

coastal environment (Zhang et al., 1985; Li, 1986). Another opinion suggests that the reddish sand dunes were transported by winds for some distances from the coast (Wu, 1996; Zhu et al., 1988; Wang et al., 1998; Shen et al., 2016). We demonstrate that the reddish coastal dunes are aeolian in origin based on the following three lines of evidence:

(1) Field investigation can provide the most direct evidence of aeolian sand dunes. The outcrop in the Junshan section clearly shows cross-bedding (Fig. 3d), which has an angle of repose of 33°. This is in the range of angle of repose of aeolian sand dunes (30 to 35°) (Atwood-Stone and McEwen, 2013), being bigger than that of cross-bedding forming in any fluvial setting (usually less than 22°). Additionally, the dune sands are poorly cemented and well sorted, being also common features of aeolian dune sands.
(2) The surface microstructures of quartz grains can be also used to examine the sediment transport history (Cardona et al., 2005; Damiani et al., 2006; Warrier et al., 2016). The sub-rounded shapes and dish-shaped depressions (Figs. 9a, b) are typical features of aeolian sands.
(3) Topography is a fundamental factor controlling sand transportation and deposition in the Qingfeng and Junshan sections. These two sections are located on the windward slopes of local hills facing the coastline (Fig. 2). The local hills reduce the wind speed and block the movement of the aeolian sand dunes. Taking the Junshan section as an example, dune sands of this section are typical climbing dunes (Fig. 11). Pye and Tsoar (2009) proposed that aeolian sediment and airflow depend on topography at all length scales in mountainous regions. Topography can decelerate airflow and form upwind obstacle of moving sands, resulting in upwind accumulations of sands (climbing dunes). The distribution of paleo-sand dunes in the Junshan section demonstrates that topography had an important influence on the sand accumulation in this area.

5.3. *Relationship between the accumulations of coastal dunes and the eustatic sea-level fluctuations*

The relationship between the evolution of coastal dunes and sea-level change has been studied and various models have been proposed (e.g., Murray-Wallace, 2002; Bateman et al., 2004, 2011; Porat and Botha, 2008; Andreucci et al., 2009; Tamura et al., 2011). Dating of coastal dunes has demonstrated that their formation is in relation to sea-level highstands (e.g., Murray-Wallace, 2002; Bateman et al., 2004, 2011; Porat and Botha, 2008; Murray-Wallace et al., 2010; Tamura et al., 2011). Meanwhile, there are several coastal dunes related to sea-level lowstands (e.g., Andreucci et al., 2009). No matter coastal dunes develop at low or high sea levels, these models all suggest that sea-level change is a trigger for coastal dune building (Ritchie, 1972; Lees, 2006), and the development of the aeolian sand dunes in coastal regions is highly coherent with marine transgression or regression processes.

The paleo-aeolian sand dunes in the coast of SE China, have been used to infer paleoclimate and sea-level changes (Zhang et al., 2008; Jin et al., 2017, 2018). These earlier studies suggest that the aeolian dunes corresponded to lower sea levels (Wu et al., 1995; Zeng et al., 1999; Wu et al., 2000; Jin et al., 2018), although some recent researchers suggest that sand accumulations could occur during higher sea levels (Jin et al., 2017).

The OSL ages of this study provide a novel chronology of aeolian sand deposition in SE China (Fig. 6). Fig. 12 shows the relationship

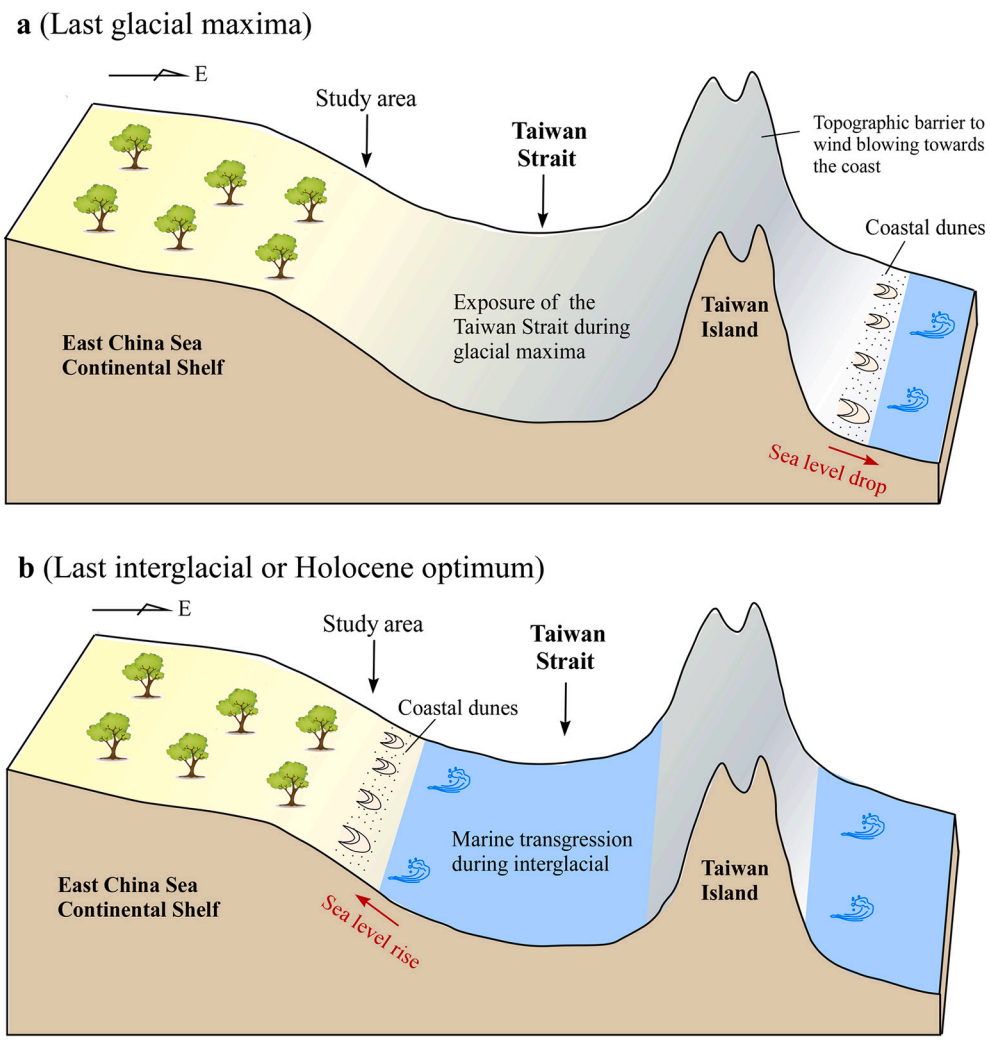

Fig. 13. Conceptual models show the evolution of aeolian sand dunes in the coastal zone of SE China. (a) Sea level drop during the last glacial maxima (MIS 4 and 2) exposed both the continental shelf and the Taiwan Strait, and the coastal sand dunes might develop in a lower elevation, but was several hundred kilometers away from the present coastline and blocked by the topographic barrier of Taiwan Island; (b) Sea level rise during the warm periods (especially for MIS 1 and 5) was favorable for the accumulation of aeolian coastal sand dunes at higher altitudes transported by prevailing winds.

between the OSL ages and the reconstructed sea-level fluctuations since the Penultimate glaciation (data from Grant et al., 2012, 2014).

Our chronologies indicate that most of the paleo-aeolian sand dunes, preserved in the study area, accumulated in three periods: 9–6 ka (broadly corresponding to MIS 1), 50–26 ka (MIS 3), and 110–74 ka (MIS 5). These stages were also periods of relative higher sea-levels compared with those in the glacial maxima due to the melting of polar ice-sheets in the warmer period (Fig. 12). Although there is an OSL age of 175.9 ± 16.9 ka, this age is a MET-pIRIR age of K-feldspar with large uncertainty. Generally, we did not find paleo-aeolian sand dunes formed during the Penultimate glacial (MIS 6) and the colder stages of the last glacial (MIS 2 and MIS 4) (Fig. 12).

We interpret the formations of the paleo-aeolian coastal dunes by using a conceptual model (Fig. 13). For the formation of sand dunes, three factors are necessary: (1) sand supply, (2) winds, and (3) preservation (e.g., Lancaster et al., 2002; Chase and Thomas, 2007; Singhvi and Porat, 2008; Jayangondaperumal et al., 2012). Such conditions for dune formation can occur both in glacial and interglacial periods in the coastal regions. In order to interpret the dune formation and preservation in the studied regions we need to have knowledge about the past sea-level fluctuations and continental shelf evolution.

It has been demonstrated that the sea-level fluctuations are controlled by the melting and growth of polar ice-sheets as well as the changing shelf-accommodation (due to tectonics and the amount and rate of sediment supply) (Pico et al., 2017). The studied region is located in a relatively stable tectonic domain of South China Block (Yin, 2010), and there is no large river diversion during the studied time scale. In such a short time, the effects of tectonic uplift and sediment supply can be negligible. The predominant factor governing sea-level changes is the glacial isostatic adjustment.

Previous studies have shown that the sea level was ~120 m lower than the present during MIS 2 (Fleming et al., 1998; Lambeck and Chappell, 2001; Clark and Mix, 2002; Osterberg, 2006; Rabineau et al., 2006) and was ~100 m lower during MIS 4 (Pico et al., 2017). The greatly exposed continental shelf due to sea-level drop in glacial stages led to the coastal dune formation (Fig. 13a). However, the studied area is located on the continental shelf of the East China Sea, facing the Taiwan Strait (Fig. 1) which has a width ranging from 130 to 360 km and a water depth of less than 60 m in 3/4 of its total area (Li et al., 2006). In this context, a sea-level drop of 100–120 m during MIS 2 and 4, led to the exposure of the Taiwan Strait and resulted in a ~ 200 to 350 km eastward retreat of the shoreline (Fig. 13a). The long distance from the shoreline, combined with the blocking of the Central Mountain Range (up to 3860 m above sea level) in Taiwan, was not favorable for the sand movement to the studied sites (Fig. 13a). Meanwhile, lower sea-level coastal dunes could be easily washed away by water waves during a subsequent marine transgression. This can account for why there are no corresponding dune sands of MIS 2 and MIS 4 preserved in the studied region.

During the periods of MIS 1 and 5, sea-level rose to the present height (MIS 1) or only up to 60–40 m lower in most time of MIS 5 (Fig. 12) driven by the melting of the polar ice-sheet. During these periods, the

Taiwan Strait was occupied by sea water, the rise of sea-level was favorable for the sand movement by winds from coastline to a higher land on the windward slope of hills, which formed climbing dune sands (Fig. 13b). During MIS 3, although the sea-level would be ~60 m lower than at present, 1/4 of the Taiwan Strait was still occupied by sea due to the fact that only 3/4 of its present area is shallower than 60 m (Li et al., 2006). Without the topographic barrier of the Taiwan Island, the coastal sands could be transported by strong winds to higher altitudes in land and thus preserved as paleo-sand dunes. In this context, the paleo-aeolian sand dunes formed in MIS 5, 3, and 1 were located at higher altitudes, they could not be washed away by water waves and thus preserved on the windward slope of hills in the coastal region of SE China.

6. Conclusions

The paleo-aeolian coastal sand dunes in southeast China provide important information about continental shelf evolution and sea-level changes since the beginning of the Penultimate glaciation. Our OSL results from two representative sites reveal that the paleo-aeolian reddish sand dunes were accumulated during the last interglacial (MIS 5), the interstadial of the last glaciation (MIS 3), and the Holocene (MIS 1). Our new results are contrary to some previous argument that the preserved reddish coastal sand dunes in SE China were formed in cold periods.

Although dune formations could occur both in glacial and interglacial times, the sand dunes formed in the glacial maxima were not preserved in the present coastal region in SE China. Such dune sands were difficult to move to higher altitudes due to the sea-level drop and the largely retreated shoreline. Moreover, these low elevation dunes might be washed away by water waves during the subsequent marine transgression. In this context, coastal dunes in higher altitudes that accumulate during higher sea-level phases could be more easily preserved, this is the case of the paleo-aeolian sand dunes in the coastal region of SE China.

Declaration of Competing Interest

The authors declare that they have no competing financial interests or personal relationships that could have appeared to influence the work reported in this paper.

Acknowledgements

This study was funded by the National Science Foundation of China (Grants 41877443, 41888101), the Strategic Priority Research Program of Chinese Academy of Sciences (XDA20070202), the Chinese Geological Survey Project (Grant DD20190306 and DD20221644). We thank the two anonymous reviewers for their helpful comments that highly improve this paper, and Professor Paul Hesse for the editorial handling of the manuscript.

References

Aitken, M.J., 1998. Introduction to Optical Dating: The Dating of Quaternary Sediments by the Use of Photon-Stimulated Luminescence. Oxford University Press, New York.
Alappat, L., Seralathan, P., Shukla, A.D., Thrivikramji, K.P., Singhvi, A.K., 2013. Chronology of red dune aggradations of South India and its Palaeo-environmental significance. Geochronometria 40, 274–282.
Andreucci, S., Pascucci, V., Murray, A.S., Clemmensen, L.B., 2009. Late Pleistocene coastal evolution of San Giovanni di Sinis, West Sardinia (Western Mediterranean). Sediment. Geol. 216, 104–116.
Atwood-Stone, C., McEwen, A.S., 2013. Avalanche slope angles in low-gravity environments from active Martian sand dunes. Geophys. Res. Lett. 40, 2929–2934.
Bailey, R.M., Stokes, S., Bray, H., 2003. Inductively-coupled plasma mass spectrometry (ICP-MS) for dose rate determination: some guidelines for sample preparation and analysis. Ancient TL 21, 11–15.
Bateman, M.D., Holmes, P.J., Carr, A.S., Horton, B.P., Jaiswal, M.K., 2004. Aeolianite and barrier dune construction spanning the last two glacial-interglacial cycles from the southern Cape coast, South Africa. Quat. Sci. Rev. 23, 1681–1698.
Bateman, M.D., Carr, A.S., Dunajko, A.C., Holmes, P.J., Roberts, D.L., McLaren, S.J., Bryant, R.G., Marker, M.E., Murray-Wallace, C.V., 2011. The evolution of coastal barrier systems: a case study of the Middle-late Pleistocene wilderness barriers, South Africa. Quat. Sci. Rev. 30, 63–81.
Besler, H., 2008. Chapter six: Quartz sand as an indicator of humid periods. Dev. Sedimentol. 59, 129–144.
Braun, J.J., Pagel, M., Herbilln, A., Rosin, C., 1993. Mobilization and redistribution of REEs and thorium in a syenitic lateritic profile: a mass balance study. Geochim. Cosmochimi. Acta 57, 4419–4434.
Buylaert, J.P., Murray, A.S., Thomsen, K.J., Jain, M., 2009. Testing the potential of an elevated temperature IRSL signal from K-feldspar. Radiat. Meas. 44, 560–565.
Cardona, J.P.M., Mas, J.M.G., Bellón, A.S., Domínguez-Bella, S., Martínez López, J., 2005. Surface textures of heavy-mineral grains: a new contribution to provenance studies. Sediment. Geol. 174, 223–235.
Carter, R.W.G., 1991. Near-future Sea level impacts on coastal dune landscapes. Landsc. Ecol. 6, 29–39.
Chabaux, F., Riotte, J., Dequincey, O., 2003. U-Th-Ra fractionation during weathering and river transport. Rev. in Mineral. Geochem. 52 (1), 533–576.
Chase, B.M., Thomas, D.S., 2007. Multiphase late Quaternary aeolian sediment accumulation in western South Africa: timing and relationship to palaeoclimatic changes inferred from the marine record. Quat. Int. 166, 29–41.
Clark, P.U., Mix, A.C., 2002. Ice sheets and sea level of the last Glacial Maximum. Quat. Sci. Rev. 21, 1–7.
Colarossi, D., Duller, G.A.T., Roberts, H.M., 2018. Exploring the behavior of luminescence signals from feldspars: Implications for the single aliquot regenerative dose protocol. Radiat. Meas. 109, 35–44.
Damiani, D., Giorgetti, G., Turbanti, I.M., 2006. Clay mineral fluctuations and surface textural analysis of quartz grains in Pliocene-Quaternary marine sediments from Wilkes Land continental rise (East-Antarctica): paleoenvironmental significance. Mar. Geol. 226, 281–295.
Dequincey, O., Chabaux, F., Clauer, N., Sigmarsson, O., Liewig, N., Leprun, J.C., 2002. Chemical mobilizations in laterites: evidence from trace elements and ^{238}U-^{234}U-^{230}Th disequilibria. Geochim. Cosmochim. Acta 66, 1197–1210.
Duller, G.A.T., 2003. Distinguishing quartz and feldspar in single grain luminescence measurements. Radiat. Meas. 37, 161–165.
Fleming, K., Johnston, P., Zwartz, D., Yokoyama, Y., Lambeck, K., Chappell, J., 1998. Refining the eustatic sea-level curve since the last Glacial Maximum using far- and intermediate-field sites. Earth Planet. Sci. Lett. 163, 327–342.
Fu, X., Li, S.-H., 2013. A modified multi-elevated-temperature post-IR IRSL protocol for dating Holocene sediments using K-feldspar. Quat. Geochron. 17, 44–54.
Fu, X., Li, B., Li, S.-H., 2012. Testing a multi-step post-IR IRSL dating method using polymineral fine grains from Chinese loess. Quat. Geochron. 10, 8–15.
Fu, X., Li, S.-H., Li, B., 2015. Optical dating of aeolian and fluvial sediments in North Tian Shan range, China: Luminescence characteristics and methodological aspects. Quat. Geochron. 30, 161–167.
Fu, X., Li, B., Jacobs, Z., Jankowski, N.R., Cohen, T.J., Roberts, R.G., 2020. Establishing standardised growth curves (SGCs) for OSL signals from individual grains of quartz: a continental-scale case study. Quat. Geochron. 60, 101–107.
Gardner, R., Pye, K., 1981. Nature, origin and paleoenvironmental significance of red coastal and desert dune sands. Progr. Phys. Geogr. 5, 514–534.
Grant, K.M., Rohling, E.J., Bar-Matthews, M., Ayalon, A., Medina-Elizalde, M., Ramsey, C.B., Satow, C., Roberts, A.P., 2012. Rapid coupling between ice volume and polar temperature over the past 150,000 years. Nature 491, 744–747.
Grant, K.M., Rohling, E.J., Bronk Ramsey, C., Cheng, H., Edwards, R.L., Florindo, F., Heslop, D., Marra, F., Roberts, A.P., Tamisiea, M.E., Williams, F., 2014. Sea-level variability over five glacial cycles. Nat. Commun. 5, 5076. https://doi.org/10.1038/ncomms6076.
Guérin, G., Mercier, N., Adamiec, G., 2011. Dose-rate conversion factors: update. Ancient TL 29, 5–8.
Hamylton, M.S., 2017. Spatial Analysis of Coastal Environments. Cambridge University Press, Cambridge.
Hansom, J.D., 2001. Coastal sensitivity to environmental change: a view from the beach. Catena 42, 291–305.
Hu, F.G., Li, Z.Z., Jin, J.H., Chen, X.L., Xia, J., Wang, X.L., 2012. A primary research on multiphase development pattern of "old red sand" in Jingjiang coast of South East Fujian. Quat. Sci. 32, 1207–1220 (in Chinese with English abstract).
Huntley, D.J., Hancock, R.G.V., 2001. The Rb contents of the K-feldspars being measured in optical dating. Ancient TL 19, 43–46.
Jayangondaperumal, R., Murari, M.K., Sivasubramanian, P., Chandrasekar, N., Singhvi, A.K., 2012. Luminescence dating of fluvial and coastal red sediments in the SE coast, India, and implications for paleoenvironmental changes and dune reddening. Quat. Res. 77, 468–481.
Jeong, G.Y., Cheong, C.S., Choi, J.H., 2007. The effect of weathering on optically stimulated luminescence dating. Quat. Geochron. 2, 117–122.
Jin, J.H., Li, Z.Z., Lei, G.L., Ling, Z.Y., Jiang, F., Shen, J.L., Liu, X.M., 2017. Chronology and envrionmental significance of old red sand in South China: take the old red sand in Qingfeng, Fujian as an example. Sci. Geogr. Sin. 37, 301–310.
Jin, J.H., Li, Z.Z., Cheng, Y., Xu, X.L., Li, Z.X., Liu, X.J., 2018. Late Pleistocene aeolian activity in Haitan Island, Southeast China: Insights from optically stimulated luminescence dating of coastal dunes on marine terraces. J. Mt. Sci. 15, 1777–1788.
Jin, J.H., Wang, X.Y., Zhou, Z.Y., Huang, Y.M., Fan, X.C., Zuo, X.X., Li, Z.Z., Ling, Z.Y., Ren, Y.Q., Li, S.T., 2021. OSL chronology of a Palaeolithic site in a humid subtropical mountainous area of Southeast China. J. Mt. Sci. 18, 2012–2023.
Kang, S.G., Wang, X.L., Li, X.N., Lu, Y.C., 2010. Anomalous fading of the IRSL signal of polymineral grains in Chinese loess. Radiat. Meas. 45, 22–28.

Kars, R.H., Reimann, T., Ankjærgaard, C., Wallinga, J., 2014. Bleaching of the post-IR IRSL signal: new insights for feldspar luminescence dating. Boreas 43, 780–791.
Lai, Z.P., 2006. Testing the use of an OSL standardised growth curve (SGC) for De determination on quartz from the Chinese Loess Plateau. Radiat. Meas. 41, 9–16.
Lai, H.C., Li, Z.Z., Jin, J.H., Deng, T., Jiang, F., Yuan, X.Q., Shen, J.L., Yu, X.L., Xu, X.L., Cheng, Y., 2017. Sedimentary structure and developing model of coastal alluvial fan along the northern coast of Haitan Island, Fujian. Acta Geol. Sin. 91, 1878–1893 (in Chinese with English abstract).
Lambeck, K., Chappell, J., 2001. Sea level change through the last glacial cycle. Science 292, 679–686.
Lancaster, N., Nickling, W.G., Neuman, C.M., 2002. Particle size and sorting characteristics of sand in transport on the stoss slope of a small reversing dune. Geomorphology 43, 233–242.
Lees, B., 2006. Timing and formation of coastal dunes in northern and eastern Australia. J. Coast. Res. 22, 78–89.
Li, J.S., 1986. Discussion on the formation of "Red Old Sand" based on one section in Dongshan Island. Mar. Sci. Bull. 5, 44–47 (in Chinese).
Li, B., Li, S.-H., 2006. Comparison of De estimates using the fast component and the medium component of quartz OSL. Radiat. Meas. 41, 125–136.
Li, B., Li, S.-H., 2011. Luminescence dating of K-feldspar from sediments: a protocol without anomalous fading correction. Quat. Geochron. 6, 468–479.
Li, B., Li, S.-H., 2012. Luminescence dating of Chinese loess beyond 130 ka using the non-fading signal from K-feldspar. Quat. Geochron. 10, 24–31.
Li, B., Li, S.-H., 2013. The effect of band-tail states on the thermal stability of the infrared stimulated luminescence from K-feldspar. J. Lumin. 136, 5–10.
Li, S.-H., Sun, J.M., Zhao, H., 2002. Optical dating of dune sands in the northeastern deserts of China. Palaeogeogr. Palaeoclimatol. Palaeoecol. 181, 419–429.
Li, C., Hu, J., Jan, S., Wei, Z., Fang, G., Zheng, Q., 2006. Winter-spring fronts in Taiwan Strait. J. Geophys. Res. 111, C11S13. https://doi.org/10.1029/2005JC003203.
Li, B., Li, S.-H., Wintle, A.G., Zhao, H., 2008. Isochron dating of sediments using luminescence of K-feldspar grains. J. Geophys. Res. 113, F02026. https://doi.org/10.1029/2007JF000900.
Li, Z.W., Li, B.S., Sun, L., Wang, F.N., Wen, X.H., Niu, D.F., 2011. Overview and prospect of research on Old Red Sand along Southeast Coast of China. J. Desert Res. 1, 49–57 (in Chinese with English abstract).
Li, B., Jacobs, Z., Roberts, R.G., Li, S.-H., 2013. Extending the age limit of luminescence dating using the dose-dependent sensitivity of MET-pIRIR signals from K-feldspar. Quat. Geochron. 17, 55–67.
Li, B., Jacobs, Z., Roberts, R.G., Li, S.-H., 2014. Review and assessment of the potential of post-IR IRSL dating methods to circumvent the problem of anomalous fading in feldspar luminescence. Geochronometria 41, 178–201.
Liu, J.F., Murray, A., Sohbati, R., Jain, M., 2016. The effect of test dose and first IR stimulation temperature on post-IR IRSL measurements on rock slices. Geochronometria 43, 179–187.
Lü, T.Y., Sun, J.M., Gong, Z.J., 2018. Optical dating of eolian deposits since the last interglacial along the northern margin of the Chinese Loess Plateau. J. Asian Earth Sci. 155, 154–163.
Madsen, D.B., Liu, X.J., 2018. Comparative post-IR IRSL (pIRIR290) K-feldspar age estimates for Qinghai Lake highstands: a comment. Quat. Geochronol. 48, 104–107.
Mathieu, D., Bernat, M., Nahon, D., 1995. Short-lived U and Th isotope distribution in a tropical laterite derived from granite (Pitinga river basin, Amazonia, Brazil): application to assessment of weathering rate. Earth Planet. Sci. Lett. 136, 703–714.
Mckee, E.D., 1979. A Study of Global Sand Seas. U. S. Geol. Surv. Prof. Pap.1052, U.S. Government Printing Office, Washington, D.C.
Mejdahl, V., Christiansen, H.H., 1994. Procedures used for luminescence dating of sediments. Quat. Sci. Rev. 13, 403–406.
Murray, A.S., Olley, J.M., 2002. Precision and accuracy in the optically stimulated luminescence dating of sedimentary quartz: a status review. Geochronometria 21, 1–16.
Murray, A.S., Wintle, A.G., 2000. Luminescence dating of quartz using an improved single-aliquot regenerative-dose protocol. Radiat. Meas. 32, 57–73.
Murray, A.S., Wintle, A.G., 2003. The single aliquot regenerative dose protocol: potential for improvements in reliability. Radiat. Meas. 37, 377–381.
Murray-Wallace, C.V., 2002. Pleistocene coastal stratigraphy, sea-level highstands and neotectonism of the southern Australian passive continental margin-a review. J. Quat. Sci. 17, 469–489.
Murray-Wallace, C.V., Bourman, R.P., Prescott, J.P., Williams, F., Price, D.M., Belperio, A.P., 2010. Aminostratigraphy and thermoluminescence dating of coastal aeolianites and the later Quaternary history of a failed delta: the River Murray mouth region, South Australia. Quat. Geochronol. 5, 28–49.
Nel, R., Campbell, E.E., Harris, L., Hauser, L., Schoeman, D.S., McLachlan, A., Preez, D. R., Bezuidenhout, K., Schlacher, T.A., 2014. The status of sandy beach science: past trends, progress, and possible futures. Estuar. Coast. Shelf Sci. 150, 1–10.
Nian, X.M., Bailey, R.M., Zhou, L.P., 2012. Investigations of the post-IR IRSL protocol applied to single K-feldspar grains from fluvial sediment samples. Radia. Meas. 47, 703–709.
Olley, J.M., Murray, A., Roberts, R.G., 1996. The effects of disequilibria in the uranium and thorium decay chains on burial dose rates in fluvial sediments. Quat. Sci. Rev. 15, 751–760.
Osterberg, E.C., 2006. Late Quaternary (marine isotope stages 6-1) seismic sequence stratigraphic evolution of the Otago continental shelf, New Zealand. Mar. Geol. 229, 159–178.
Pico, T., Creveling, J.R., Mitrovica, J.X., 2017. Sea-level records from the U. S. Mid-Atlantic constrain Laurentide Ice Sheet extent during Marine Isotope Stage 3. Nat. Commun. 8, 15612. https://doi.org/10.1038/ncomms15612.
Porat, N., Botha, G., 2008. The luminescence chronology of dune development on the Maputaland coastal plain, Southeast Africa. Quat. Sci. Rev. 27, 1024–1046.
Prescott, J.R., Hutton, J.T., 1994. Cosmic ray contributions to dose rates for luminescence and ESR dating: large depths and long-term time variations. Radiat. Meas. 23, 497–500.
Prescott, J.R., Stephan, L.G., 1982. The contribution of cosmic radiation to the environmental dose for thermoluminescence dating. Latitude, altitude and depth dependences. Pact 6, 17–25.
Pye, K., Tsoar, H., 2009. Aeolian Sand and Sand Dunes. Springer, Berlin.
Qin, J.T., Zhou, L.P., 2012. Effects of thermally transferred signals in the post-IR IRSL SAR protocol. Radiat. Meas. 47, 710–715.
Quang-Minh, D., Frechen, M., Nghi, T., Harff, J., 2010. Timing of Holocene sand accumulation along the coast of central and SE Vietnam. Int. J. Earth Sci. 99, 1731–1740.
Rabineau, M., Berné, S., Olivet, J.-L., Aslanian, D., Guillocheau, F., Joseph, P., 2006. Paleo Sea levels reconsidered from direct observation of paleoshoreline position during Glacial Maxima (for the last 500,000 yr). Earth Planet. Sci. Lett. 252, 119–137.
Ritchie, W., 1972. The evolution of coastal sand dunes. Scot. Geog. Mag. 88 (1), 19–35.
Roberts, H.M., 2012. Testing Post-IR IRSL protocols for minimising fading in feldspars, using Alaskan loess with independent chronological control. Radiat. Meas. 47, 716–724.
Roskin, J., Dan, G.B., Porat, N., Tsoar, H., Rozenstein, O., 2012. Do dune sands redden with age? The case of the northwestern Negev dunefield, Israel. Aeolian Res. 5, 63–75.
Rust, I.C., Illenberger, W.K., 1996. Coastal dunes: sensitive or not? Landsc. Urban Plan. 34, 165–169.
Shen, J.L., Li, Z.Z., Jin, J.H., Deng, T., Jiang, F., Yuan, X.Q., Yu, X.L., Lai, H.C., 2016. Grain-size characteristics and the paleoenvironmental significance of the cyclically deposited "Old Red Sand" in Qingfeng, Haitan Island, Fujian. China. J. Desert Res. 36, 972–982 (in Chinese with English abstract).
Singhvi, A.K., Porat, N., 2008. Impact of luminescence dating on geomorphological and palaeoclimate research in drylands. Boreas 37, 536–558.
Singhvi, A., Deraniyagala, S., Sengupta, D.J.E., Letters, P.S., 1986. Thermoluminescence dating of Quaternary red-sand beds: a case study of coastal dunes in Sri Lanka. Earth Planet. Sci. Lett. 80, 139–144.
Steffen, D., Preusser, F., Schlunegger, F., 2009. OSL quartz age underestimation due to unstable signal components. Quat. Geochronol. 4, 353–362.
Tamura, T., Kodama, Y., Bateman, M.D., Saitoh, Y., Watanabe, K., Matsumoto, D., Yamaguchi, N., 2011. Coastal barrier dune construction during sea-level highstands in MIS 3 and 5a on Tottori coastline, Japan. Palaeogeogr. Palaeoclimatol. Palaeoecol. 308, 492–501.
Tan, H.Z., Wu, Z., 2001. TL Dating of the "Old Red Sand" on the Coasts of Fujian and Guangdong. J. Desert Res. 21, 393–396 (in Chinese with English abstract).
Thiel, C., Buylaert, J.P., Murray, A.G., Terhorst, B., Hofer, I., Tsukamoto, S., Frechen, M., 2011. Luminescence dating of the Stratzing loess profile (Austria)–Testing the potential of an elevated temperature post-IR IRSL protocol. Quat. Int. 234, 23–31.
Tsoar, H., Blumberg, D.G., Wenkart, R., 2008. Formation and geomorphology of the NW Negev Sand Dunes. In: Breckle, S.W., Yair, A., Veste, M. (Eds.), Arid Dune Ecosystems. Springer, Berlin, pp. 25–48.
Tsoar, H., Levin, N., Porat, N., Maia, L.P., Herrmann, H., Tatumi, S.H., Claudino-Sales, V., 2009. The effect of climate change on the mobility and stability of coastal sand dunes in Ceara State (NE Brazil). Quat. Res. 71, 217–226.
Walker, T.R., 1979. Red color in dune sand. In: MaKee, E.D. (Ed.), A Study of Global Sand Seas. U.S. Geol. Surv. Prof. Pap. 1052. United States Goverment Printing Office, Washington, pp. 61–81.
Wang, J.H., Liang, Z.R., Zheng, Z., Chen, S.X., 1998. Some proof about eolian origin of Quaternary old red sands in eastern Guangdong and Northeastern Hainan. Trop. Ocean. 17, 51–58 (in Chinese with English abstract).
Wang, H., Li, Z.Z., Tian, M.Z., 2013. Envrionmental magnetism characteristics and paleoclimatic significance of the old red sandy sediment in Haitan Island of Fujian. J. Arid Land Res. Environ. 27, 122–128.
Wang, X.L., Wintle, A.G., Adamiec, G., 2014. Post-IR IRSL production in perthitic feldspar. Radiat. Meas. 64, 1–8.
Warrier, A.K., Pednekar, H., Mahesh, B.S., Mohan, R., Gazi, S., 2016. Sediment grain size and surface textural observations of quartz grains in late quaternary lacustrine sediments from Schirmacher Oasis. East Antarctica: Paleoenvironmental significance. Polar Sci. 10, 89–100.
Williams, C.H., David, D.J., Lismma, O., 1962. The determination of chromic oxide in faeces samples by atomic absorption spectrophotometry. J. Agric. Sci. 59, 381–385.
Wintle, A.G., Murray, A.S., 2006. A review of quartz optically stimulated luminescence characteristics and their relevance in single-aliquot regeneration dating protocols. Radiat. Meas. 41, 369–391.
Woodroffe, C.D., 2002. Coasts: Form, Process and Evolution. Cambridge University Press, Cambridge.
Wopfner, G., Twidale, C.R., 1988. Formation and age of desert dunes in the Lake Eyre depocentres in Central Australia. Geol. Rundsch. 77, 815–834.
Wu, Z., 1996. Research on some questions concerning South China coastal dunes. J. South China Norm. Univ. (Nat. Sci.) 1, 91–98 (in Chinese with English abstract).
Wu, Z., Wang, W., 2001. Finding and its significance of "Old Red Sand" strata with multiple depositional stages on the coasts of Fujian and Guangdong. J. Desert Res. 21, 328–332 (in Chinese with English abstract).
Wu, Z., Huang, S., Hu, S.Z., 1995. Research on the Landforms of the Wind-Drift Sand in South China Coast. Science Press, Beijing (in Chinese).
Wu, Z., Tan, H.Z., Xu, T.F., 2000. The age of the "old red sand" on the coasts of South Fujian and West Guangdong. China. Chin. Sci. Bull. 45, 533–537.

Yao, Q.Y., Zhang, H.N., Zhang, J.W., Zhao, X.T., 1985. A preliminary study on the late pleistocene stratigraphy along the coastal areas of southern Fujian. Seismol. Geol. 7, 32–40.
Yin, A., 2010. Cenozoic tectonic evolution of Asia: a preliminary synthesis. Tectonophysics 488, 293–325.
Yu, M.T., Zhang, H.Y., Gong, Z.Q., Chen, Y.X., Wang, J.W., Zhang, Y., Hu, S.J., Wu, H., 2014. The monsoon components in Qingfeng Old Red Sands and their formation epoch, Pingtan Island, Fujian Province. Sci. Geogr. Sin. 34, 352–357.
Zeng, C.S., Chen, J.C., Wu, Y.G., 1999. Sedimentary stratum and forming age of the "Old Red Sand" along the coast of Southeastern Fujian. J. Desert Res. 19, 338–342 (in Chinese with English abstract).
Zhang, J.J., Li, S.-H., 2020. Review of the post-IR IRSL dating protocol of K-feldspar. Methods. Protoc. 3, 7.
Zhang, H.N., Yao, Q.Y., Zhao, X.T., 1985. Formation and age of "Old Red San" in the coastal ages of South Fujian and East Guangdong. Mar. Geol. Quat. Geol. 5, 47–57 (in Chinese with English abstract).
Zhang, J.F., Yuan, B.Y., Zhou, L.P., 2008. Luminescence chronology of "Old Red Sand" in Jinjiang and its implications for optical dating of sediments in South China. Chin. Sci. Bull. 53, 591–601.
Zhang, J.F., Li, Y.Y., Han, Y.S., Wang, J.K., 2019. Luminescence dating of weathered sediments from the Paleolithic site of Fengshuzui in northern Hunan province. China. Quat. Geochronol. 49, 211–217.
Zhao, H., Li, S.-H., 2005. Internal dose rate to K-feldspar grains from radioactive elements other than potassium. Radiat. Meas. 40, 84–93.
Zhu, X.N., Wu, Z., Zhou, Z.Q., Wang, W., 1988. Further research on the formation of the "Old Red Sandy Sediment" along the eastern coast of Guangdong Province. Trop. Ocean. 7, 46–54 (in Chinese with English abstract).